

# Tundra uptake of atmospheric elemental mercury drives Arctic mercury pollution

Daniel Obrist<sup>1,2</sup>, Yannick Agnan<sup>2,3</sup>, Martin Jiskra<sup>4</sup>, Christine L. Olson<sup>2</sup>, Dominique P. Colegrove<sup>5</sup>, Jacques Hueber<sup>5</sup>, Christopher W. Moore<sup>2,6</sup>, Jeroen E. Sonke<sup>4</sup> & Detlev Helmig<sup>5</sup>

**Anthropogenic activities have led to large-scale mercury (Hg) pollution in the Arctic<sup>1–6</sup>. It has been suggested that sea-salt-induced chemical cycling of Hg (through ‘atmospheric mercury depletion events’, or AMDEs) and wet deposition via precipitation are sources of Hg to the Arctic in its oxidized form (Hg(II)). However, there is little evidence for the occurrence of AMDEs outside of coastal regions, and their importance to net Hg deposition has been questioned<sup>2,7</sup>. Furthermore, wet-deposition measurements in the Arctic showed some of the lowest levels of Hg deposition via precipitation worldwide<sup>8</sup>, raising questions as to the sources of high Arctic Hg loading. Here we present a comprehensive Hg-deposition mass-balance study, and show that most of the Hg (about 70%) in the interior Arctic tundra is derived from gaseous elemental Hg (Hg(0)) deposition, with only minor contributions from the deposition of Hg(II) via precipitation or AMDEs. We find that deposition of Hg(0)—the form ubiquitously present in the global atmosphere—occurs throughout the year, and that it is enhanced in summer through the uptake of Hg(0) by vegetation. Tundra uptake of gaseous Hg(0) leads to high soil Hg concentrations, with Hg masses greatly exceeding the levels found in temperate soils. Our concurrent Hg stable isotope measurements in the atmosphere, snowpack, vegetation and soils support our finding that Hg(0) dominates as a source to the tundra. Hg concentration and stable isotope data from an inland-to-coastal transect show high soil Hg concentrations consistently derived from Hg(0), suggesting that the Arctic tundra might be a globally important Hg sink. We suggest that the high tundra soil Hg concentrations might also explain why Arctic rivers annually transport large amounts of Hg to the Arctic Ocean<sup>9–11</sup>.**

The levels and impacts of mercury pollution are increasingly being modulated by climate-change-induced disturbances in aquatic and terrestrial biogeochemistry<sup>12</sup>, with potentially the most notable consequences being seen in the Arctic, where warming occurs at a rate almost double the worldwide average<sup>13,14</sup>. Regulatory frameworks such as the recent Minamata Convention of the United Nations Environment Programme—aimed at reducing Hg pollution globally<sup>15</sup>—rely on a clear understanding of Hg sources, which is lacking at present in the Arctic. The widespread Hg pollution observed across the Arctic is inconsistent with the extremely low atmospheric wet deposition, which in Arctic ecosystems is among the lowest globally. For example, the annual wet mercury deposition rate of  $2.1 \pm 0.7 \mu\text{g m}^{-2} \text{yr}^{-1}$  at Gates of the Arctic National Park in Alaska (Supplementary Table 1) is only one-fifth of the wet deposition measured across 99 lower-latitude US locations ( $9.7 \pm 3.9 \mu\text{g m}^{-2} \text{yr}^{-1}$ )<sup>8</sup>. Also unclear are the origins of the vast amounts of Hg that are transferred annually by Arctic rivers to the Arctic Ocean<sup>9</sup>. These riverine Hg inputs to the Arctic Ocean, which exceed direct atmospheric deposition<sup>10,11</sup>, stand in contrast to predictions that rank Arctic catchments lowest in terms

of watershed Hg storage globally<sup>16</sup>. Another potential Hg source—deposition resulting from sea-salt-induced AMDEs in springtime<sup>17</sup>—was long thought to be responsible for high Arctic Hg deposition. However, AMDEs may cause little net Hg deposition because most of the deposited Hg can revolatilize into the atmosphere before the snow melts, and studies provide inconclusive evidence about the importance of AMDEs to Arctic deposition<sup>2,7</sup>.

Unlike wet deposition and deposition related to AMDEs, both of which are composed of oxidized Hg (Hg(II)), deposition of gaseous elemental Hg(0)—the form that is subject to long-range atmospheric transport and global atmospheric distribution—is largely unconstrained and has not been measured by deposition networks. We recently reviewed<sup>18</sup> 132 studies of gaseous Hg(0) exchange between the atmosphere and terrestrial surfaces, and found that net global terrestrial Hg(0) exchange exhibits a wide range and large uncertainty, from a net deposition of  $500 \text{ Mg yr}^{-1}$  globally to a net emission (that is, volatilization from ecosystems to the atmosphere) of  $1,650 \text{ Mg yr}^{-1}$ . The large uncertainty stems from an almost complete lack of year-long and whole-ecosystem measurements of Hg(0) exchange among these studies.

Here we performed a mass-balance analysis of atmospheric Hg deposition in the Arctic tundra—a biome covering some 6% of the global land surface area—to determine the major Hg sources in one of the most remote ecosystems worldwide. We conducted a two-year field measurement campaign (Extended Data Fig. 1) to constrain atmospheric Hg deposition at Toolik Field Station on the North Slope of Alaska, USA, 200 km inland from the coast and representing the interior tundra. We measured net gaseous Hg(0) exchange at the ecosystem level using micrometeorological techniques; we also measured wet and dry Hg(II) deposition, as well as vegetation Hg inputs from aboveground biomass. We concurrently measured Hg stable-isotopic signatures in the atmosphere, snowpack, vegetation, and soil, and quantified the total mass of Hg sequestered in tundra snowpack, plants, and soils. We further measured atmosphere–snow–soil Hg(0) gas-concentration profiles, to independently verify Hg(0) exchange and to locate zones of atmospheric Hg(0) sources and sinks.

We found that gaseous Hg(0) was the dominant form of Hg deposition ( $6.5 \pm 0.7 \mu\text{g m}^{-2} \text{yr}^{-1}$ ), accounting for 71% of total deposition (Fig. 1). Wet Hg(II) deposition amounted to less than 5% of Hg(0) deposition (Supplementary Table 2;  $0.2 \pm 0.1 \mu\text{g m}^{-2} \text{yr}^{-1}$ ) and was even lower than previous low measurements from another Arctic site in Alaska<sup>8</sup>. Atmospheric Hg(II) concentrations were below the detection limit ( $33 \text{ pg m}^{-3}$ ) during most of the measured period, with the exception of March and early April during AMDEs, when concentrations reached nearly  $0.5 \text{ ng m}^{-3}$  (Extended Data Figs 2, 3). We constrained atmospheric Hg(II) dry deposition to  $2.5 \mu\text{g m}^{-2} \text{yr}^{-1}$  (range  $0.8\text{--}2.8 \mu\text{g m}^{-2} \text{yr}^{-1}$ ) on the basis of periodic measurements of atmospheric Hg(II) concentrations (Extended Data Fig. 2). We

<sup>1</sup>Department of Environmental, Earth and Atmospheric Sciences, University of Massachusetts, Lowell, Massachusetts 01854, USA. <sup>2</sup>Division of Atmospheric Sciences, Desert Research Institute, 2215 Raggio Parkway, Reno, Nevada 89512, USA. <sup>3</sup>Milieux Environnementaux, Transferts et Interactions dans les Hydrosystèmes et les Sols (METIS), UMR 7619, Sorbonne Universités UPMC-CNRS-EPHE, 4 place Jussieu, F-75252 Paris, France. <sup>4</sup>Géosciences Environnement Toulouse, CNRS/OMP/Université de Toulouse, 14 Avenue Edouard Belin, 31400 Toulouse, France. <sup>5</sup>Institute of Arctic and Alpine Research (INSTAAR), University of Colorado, 4001 Discovery Drive, Boulder, Colorado 80309, USA. <sup>6</sup>Gas Technology Institute (GTI), 1700 South Mount Prospect Road, Des Plaines, Illinois 60018, USA.

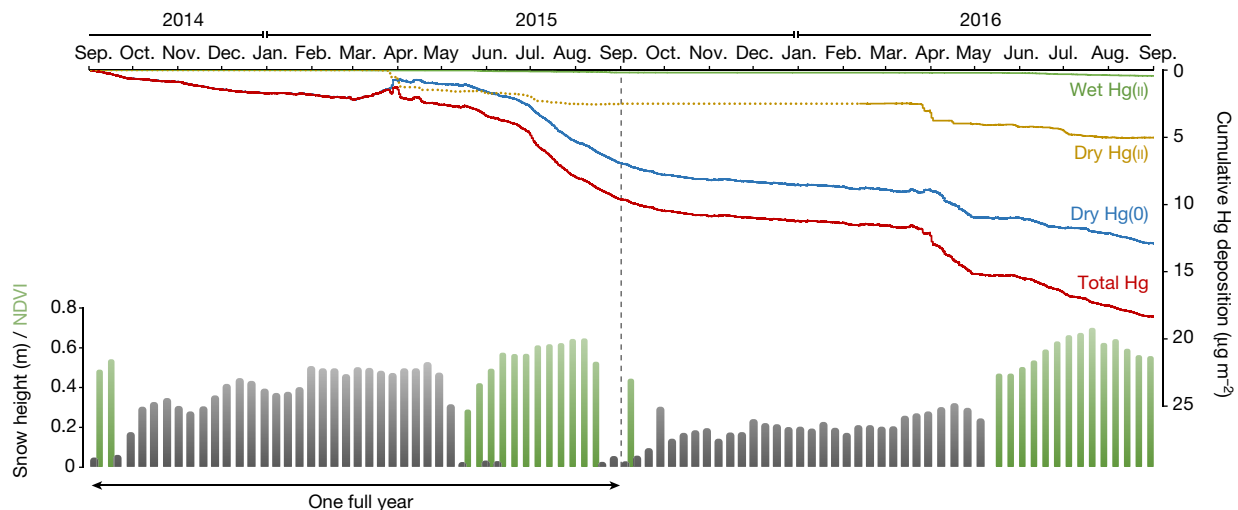


**Figure 1 | Cumulative atmospheric deposition of major Hg forms in the Arctic tundra.** Top: blue line, gaseous Hg(0) flux; green line, wet Hg(II) deposition; brown line, dry deposition of Hg(II) (dashed line

shows observations extrapolated when not measured); red line, total Hg deposition. Bottom: snow heights (grey bars) and vegetation coverage (NDVI, normalized difference vegetation index; green bars).

observed temporarily elevated snow Hg levels during springtime AMDEs, although the deposited Hg revolatilized to the atmosphere within days (Supplementary Information).

The dominance of gaseous Hg(0) deposition as a source to this ecosystem was independently confirmed by Hg stable isotope analyses. We comprehensively characterized the Hg stable isotope composition of atmospheric Hg(0), snowfall and snowpack, vegetation, organic and mineral soil horizons, and bedrock samples. As observed previously<sup>19–24</sup>, atmospheric Hg(0) and Hg(II), bedrock Hg(II), and

Hg(II) deposited through AMDEs have unique  $\delta^{202}\text{Hg}$ ,  $\Delta^{199}\text{Hg}$ , and  $\Delta^{200}\text{Hg}$  signatures (Fig. 2, Extended Data Figs 4, 5 and Extended Data Tables 1–5). We then quantified the relative contributions of different Hg sources to vegetation and soil samples using endmember mixing models and triple isotopic signatures. The results show that atmospheric gaseous Hg(0) is the dominant source of Hg in vegetation (median 90%), organic soils (73%), and upper mineral soils (55%) (Supplementary Table 3). Hg(II) wet deposition accounted for 10% to 22% of Hg in the two soil compartments; and residual Hg(II) from

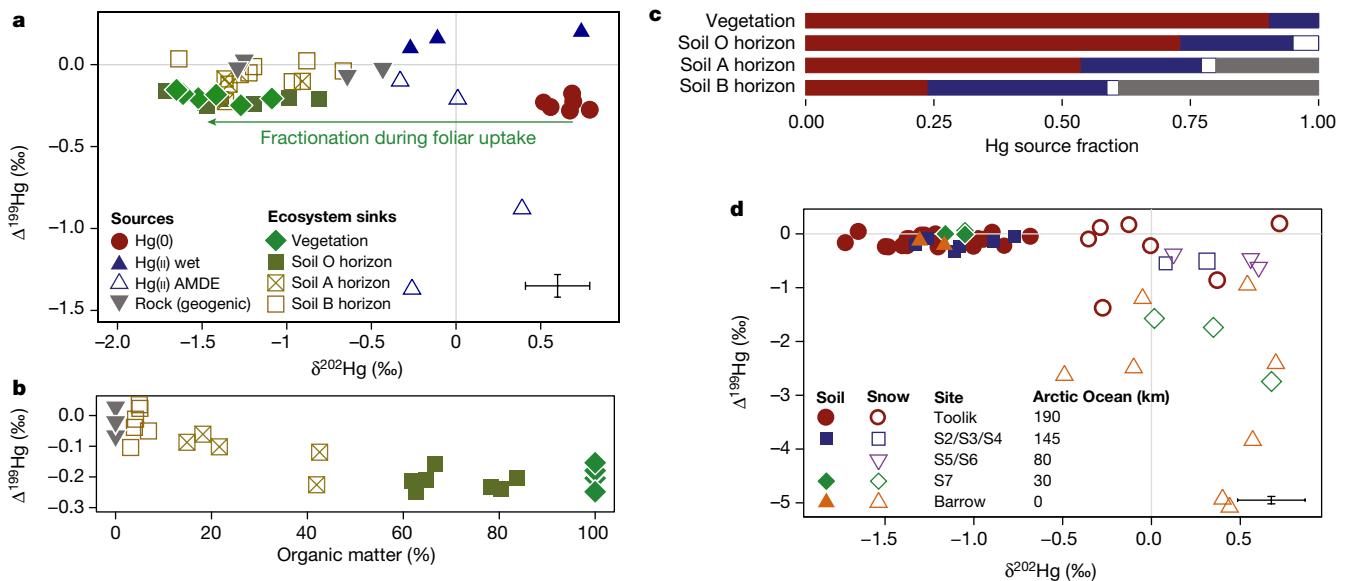


**Figure 2 | Hg stable isotope composition of atmospheric Hg(0) and Hg in snowfall and snowpack, vegetation, organic and mineral soil horizons, and bedrock samples in the Arctic tundra.** **a**, Mass-dependent ( $\delta^{202}\text{Hg}$ ) and mass-independent ( $\Delta^{199}\text{Hg}$ ) mercury isotope signatures in the tundra. Uncertainty (2 s.d. of replicate standards) is shown on the lower right. Sources: filled circles, atmospheric Hg(0); filled blue triangles, Hg(II) in snow deposited before February 2016; open triangles, Hg(II) measured in surface snow during periods of AMDEs (March to April 2016); filled inverted triangles, geogenic Hg in rock samples. Tundra samples (ecosystem sinks): filled diamonds, bulk vegetation; filled squares, organic (O horizon) soils; open squares, mineral soils (with crosses for A horizons (more than 10% organic matter) and without crosses for B horizons (less than 10% organic matter)). The arrow represents the mass-dependent fractionation of atmospheric Hg(0) during foliar

uptake. **b**, Scatterplot of  $\Delta^{199}\text{Hg}$  with organic matter content, showing that signatures of terrestrial samples can be explained predominantly by binary mixing of the two endmembers geogenic Hg and vegetation Hg. **c**, Fraction of respective Hg sources in vegetation and soil O, A and B horizons on the basis of a mixing model. Colours represent the following sources: red for atmospheric Hg(0); blue for wet Hg(II) deposition; white for Hg(II) deposition by AMDEs; and grey for geogenic Hg. **d**,  $\delta^{202}\text{Hg}$  and  $\Delta^{199}\text{Hg}$  isotope signatures of soils (filled symbols) (O, A and B horizons) and snow (open symbols) (collected during March and April) along an inland-to-coastal transect. The distance from the Arctic Ocean is given in kilometres. The data for Barrow samples are from refs 23 and 24. Measurement uncertainties, calculated as 2 s.d. of replicate standards, are shown on the lower right.

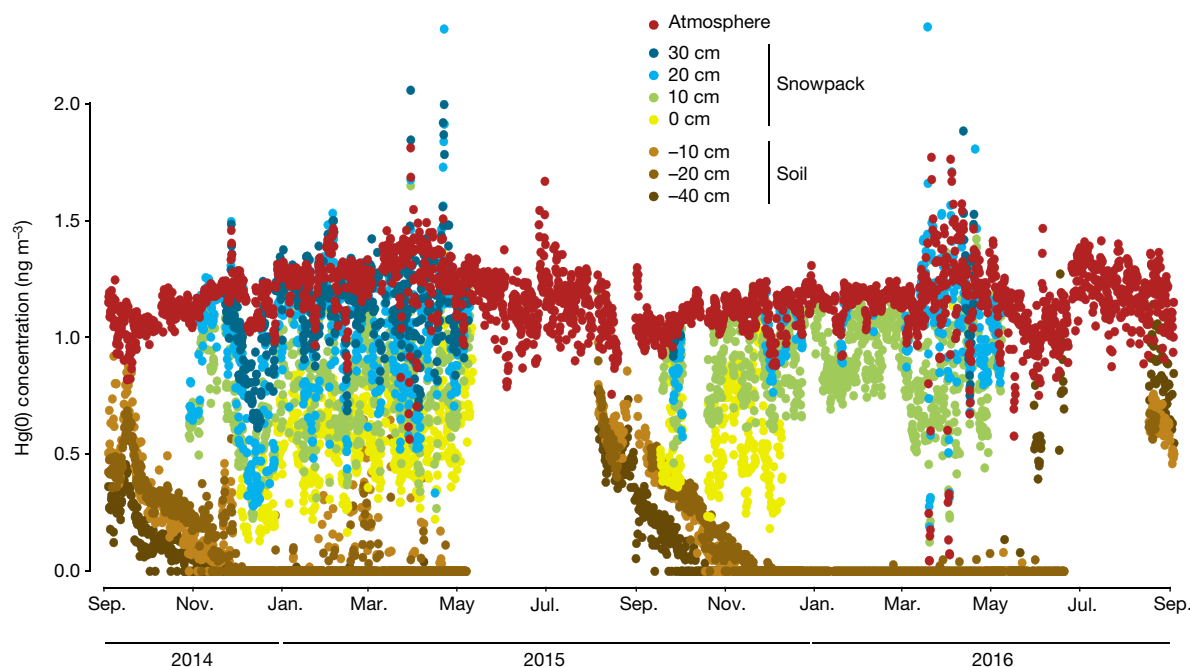


**Figure 3 | Gaseous Hg(0) concentrations in the atmosphere, interstitial snow air, and tundra soil pores.** Differently coloured symbols represent different heights above the ground surface for snowpack, and different depths of soil pores below the ground surface for soils. Zero values in soils

denote concentration measurements below detection limits. Each data point represents a six-hour mean of air, snowpack air, and soil pore air measurements.

AMDEs, transferred to the tundra soils after snowmelt, accounted for 0%–5%. Geogenic Hg contributed in the range of 0% in organic soil horizons to around 40% in mineral soil horizons. These results confirm direct flux measurements demonstrating that gaseous Hg(0) deposition is the dominant source of mercury to the tundra at Toolik Field Station. We measured soil Hg stable isotope signatures in three additional tundra sites along a transect from Toolik Field Station to the Arctic Ocean (Fig. 2d), and considered values from an additional peat profile from Barrow at the coast<sup>24</sup>; we found no statistically significant differences in isotope signatures between these soils and soils at Toolik Field Station. We hence observed no higher contributions of AMDEs (maximum 5%) even in soils closer to the coast, and found that the source of Hg in tundra soils is consistently and predominantly atmospheric Hg(0) uptake.

Continuous flux measurements allowed us to determine temporal patterns of Hg(0) deposition. Gaseous Hg(0) deposition persisted throughout periods of snow cover (Fig. 1), except in March and April when net emission of Hg(0) to the atmosphere was observed after AMDEs. From October to mid-May, Hg(0) deposition averaged  $0.4 \pm 0.4 \text{ ng m}^{-2} \text{ h}^{-1}$  and accounted for 37% of total annual Hg(0) deposition. Gaseous Hg(0) concentration profiles in snow and soil air, measured with complementary trace-gas systems (see Methods), confirmed that wintertime Hg(0) deposition occurred (Fig. 3). Hg(0) concentrations within the air of snowpack pore spaces were consistently below atmospheric concentrations, and pore-air concentrations decreased further from the upper to the lower snowpack, such that concentrations at the soil–snow interface were less than 50% of atmospheric levels. Given that diffusive and advective trace-gas fluxes are a function of respective concentration gradients, these Hg(0) concentration profiles in snowpack are consistent with a net atmospheric deposition flux of gaseous Hg(0) to the tundra ecosystem, providing a third means of verifying atmospheric Hg(0) deposition. Further analysis showed that the wintertime Hg(0) deposition was driven by a sink below the Arctic snowpack, most likely by uptake of Hg(0) in the tundra soil (see Supplementary Information). Such a soil Hg(0) sink has previously been observed in a temperate soil, but the mechanism for soil Hg(0) uptake remains unclear<sup>25</sup>.

During snow-free periods from mid-May to the end of September, Hg(0) deposition increased (to a rate of  $1.4 \pm 1.0 \text{ ng m}^{-2} \text{ h}^{-1}$ ) and continued to greatly exceed deposition of all other forms of Hg combined (contributing 78% of total summertime deposition). In fact, some of the strongest Hg(0) deposition occurred after the spring onset of the tundra vegetation growing season, indicating that tundra vegetation amplified gaseous Hg(0) deposition. Clearly identifiable by its Hg isotope signature (Fig. 2), Hg in aboveground vegetation was indeed primarily (90%) derived from atmospheric Hg(0) uptake, as shown previously<sup>19,21</sup>. We calculated substantial Hg mass contained in aboveground vegetation ( $29 \mu\text{g m}^{-2}$ ; Supplementary Table 4); this Hg can subsequently be transferred to tundra soils via plant senescence and litterfall.

The dominant and time-extended atmospheric deposition of gaseous Hg(0) to the Arctic tundra has implications for local, regional and global Hg cycling. Deposition of globally ubiquitous gaseous Hg(0) leads to unexpectedly high Hg levels in these remote tundra soils. Given the results of <sup>14</sup>C age dating, which show that the deeper soils at Toolik Field Station are older than 7,300 years (Supplementary Table 5), the deposition of atmospheric Hg(0) and accumulation of Hg in the soil profile must have occurred over millennia. Soil Hg concentrations in the active layer above the permafrost averaged  $138 \pm 15 \mu\text{g kg}^{-1}$  in organic soil layers and  $97 \pm 13 \mu\text{g kg}^{-1}$  in mineral soil horizons (Supplementary Table 5), exceeding by several times the 20–50  $\mu\text{g kg}^{-1}$  range observed across temperate and tropical soils<sup>26–28</sup>. Riverine studies suggest that substantial contributions by upland soil sources in the Arctic are needed in order to explain high Hg loadings in rivers<sup>9,10</sup>. The high tundra soil Hg levels, derived from Hg(0) uptake, might explain the conundrum that watersheds with some of the lowest Hg wet-deposition loads on Earth and with limited impacts from AMDEs show elevated Hg in rivers and widespread Hg impacts on Arctic wildlife, including in the Arctic ocean<sup>3–6</sup>.

At the global scale, the Arctic tundra serves as an important repository for atmospheric Hg(0) emitted at mid-latitudes. Stable isotope analysis across four different tundra soils along a 200-km transect on the North Slope of Alaska (Fig. 2d) confirms that atmospheric Hg(0) dominates as a source, and suggests a large-scale Hg(0) sink across the Arctic tundra. Although few soil tundra Hg concentrations have



been reported elsewhere, our measurements along this northern Alaska transect and a few published data also show high soil Hg concentrations (Supplementary Table 6). If the soil Hg pool of 27 mg m<sup>-2</sup> at Toolik Field Station (Supplementary Table 5; top 40 cm) is representative of the global tundra belt, then Arctic tundra soils might contain around 143 Gg of Hg, which would account for a third to a half of the total estimated global soil Hg pool size of 300–500 Gg (on the basis of temperate studies for this soil depth<sup>16,29</sup>). Further, our study provides an independent experimental verification of source attribution by means of Hg isotope signatures, which at this tundra site show that Hg stored in vegetation and soils is predominantly derived from atmospheric Hg(0), consistent with our direct deposition measurements. Recent Hg stable isotope studies have suggested that gaseous Hg(0) deposition may dominate as a source in remote forests of the mid-latitudes<sup>19,20,22</sup> as well. We hence call upon regulators and the scientific community to reorganize deposition monitoring<sup>30</sup> to include deposition of Hg(0), which we expect to dominate as a source across remote ecosystems worldwide.

**Online Content** Methods, along with any additional Extended Data display items and Source Data, are available in the online version of the paper; references unique to these sections appear only in the online paper.

**Received 30 January; accepted 24 May 2017.**

- Fitzgerald, W. F. *et al.* Modern and historic atmospheric mercury fluxes in northern Alaska: global sources and Arctic depletion. *Environ. Sci. Technol.* **39**, 557–568 (2005).
- Douglas, T. A. *et al.* The fate of mercury in Arctic terrestrial and aquatic ecosystems, a review. *Environ. Chem.* **9**, 321–355 (2012).
- Arctic Monitoring and Assessment Programme. *Mercury in the Arctic* (AMAP, Oslo, 2011).
- Dietz, R. *et al.* Time trends of mercury in feathers of West Greenland birds of prey during 1851–2003. *Environ. Sci. Technol.* **40**, 5911–5916 (2006).
- Dietz, R. *et al.* Trend in mercury in hair of Greenlandic polar bears (*Ursus maritimus*) during 1892–2001. *Environ. Sci. Technol.* **40**, 1120–1125 (2006).
- Outridge, P. M. *et al.* A comparison of modern and pre-industrial levels of mercury in the teeth of *Beluga* in the Mackenzie Delta, Northwest Territories, and *Walrus* at Igloodik, Nunavut, Canada. *Arctic* **55**, 123–132 (2002).
- Johnson, K. P. *et al.* Investigation of the deposition and emission of mercury in arctic snow during an atmospheric mercury depletion event. *J. Geophys. Res.* **113**, D17304 (2008).
- National Atmospheric Deposition Program. *Annual Data, all MDN sites*. <http://nadp.sws.uiuc.edu/data/mdn/annual.aspx> (accessed Oct 3, 2016).
- Schuster, P. F. *et al.* Mercury export from the Yukon river basin and potential response to a changing climate. *Environ. Sci. Technol.* **45**, 9262–9267 (2011).
- Fisher, J. A. *et al.* Riverine source of Arctic Ocean mercury inferred from atmospheric observations. *Nat. Geosci.* **5**, 499–504 (2012).
- Dastoor, A. P. & Durnford, D. A. Arctic Ocean: is it a sink or a source of atmospheric mercury? *Environ. Sci. Technol.* **48**, 1707–1717 (2014).
- Krabbenhoft, D. & Sunderland, E. M. Global change and mercury. *Science* **341**, 1457–1458 (2013).
- Polyakov, I. V. *et al.* Observationally based assessment of polar amplification of global warming. *Geophys. Res. Lett.* **29**, 1878 (2002).
- Arctic Climate Impact Assessment. *Impacts of a Warming Arctic: Arctic Climate Impact Assessment Overview Report* (Cambridge Univ. Press, 2004).
- Selin, N. E. Global change and mercury cycling: challenges for implementing a global treaty. *Environ. Toxicol. Chem.* **33**, 1202–1210 (2014).
- Smith-Downey, N. V., Sunderland, E. M. & Jacob, D. J. Anthropogenic impacts on global storage and emissions of mercury from terrestrial soils: insights from a new global model. *J. Geophys. Res. Biogeosci.* **115**, G03008 (2010).
- Steffen, A. *et al.* A synthesis of atmospheric mercury depletion event chemistry in the atmosphere and snow. *Atmos. Chem. Phys.* **8**, 1445–1482 (2008).
- Agnan, Y. *et al.* New constraints on terrestrial surface-atmosphere fluxes of gaseous elemental mercury using a global database. *Environ. Sci. Technol.* **50**, 507–524 (2016).
- Demers, J. D., Blum, J. D. & Zak, D. R. Mercury isotopes in a forested ecosystem: implications for air-surface exchange dynamics and the global mercury cycle. *Glob. Biogeochem. Cycles* **27**, 222–238 (2013).
- Jiskra, M. *et al.* Mercury deposition and re-emission pathways in boreal forest soils investigated with Hg isotope signatures. *Environ. Sci. Technol.* **49**, 7188–7196 (2015).
- Enrico, M. *et al.* Atmospheric mercury transfer to peat bogs dominated by gaseous elemental mercury dry deposition. *Environ. Sci. Technol.* **50**, 2405–2412 (2016).
- Zheng, W., Obrist, D., Weis, D. & Bergquist, B. A. Mercury isotope compositions across North American forests. *Glob. Biogeochem. Cycles* **30**, 1475–1492 (2016).
- Sherman, L. S. *et al.* Mass-independent fractionation of mercury isotopes in Arctic snow driven by sunlight. *Nat. Geosci.* **3**, 173–177 (2010).
- Biswas, A. *et al.* Natural mercury isotope variation in coal deposits and organic soils. *Environ. Sci. Technol.* **42**, 8303–8309 (2008).
- Obrist, D., Pokharel, A. K. & Moore, C. Vertical profile measurements of soil air suggest immobilization of gaseous elemental mercury in mineral soil. *Environ. Sci. Technol.* **48**, 2242–2252 (2014).
- Obrist, D. *et al.* Mercury distribution across 14 U.S. Forests. Part I: spatial patterns of concentrations in biomass, litter, and soils. *Environ. Sci. Technol.* **45**, 3974–3981 (2011).
- Smith, D. B. *et al.* Geochemical and mineralogical data for soils of the coterminous United States. *US Geological Survey Data Series* **801**, <https://pubs.usgs.gov/ds/801/> (2013).
- Amos, H. M. *et al.* Observational and modeling constraints on global anthropogenic enrichment of mercury. *Environ. Sci. Technol.* **49**, 4036–4047 (2015).
- Hararuk, O., Obrist, D. & Luo, Y. Modelling the sensitivity of soil mercury storage to climate-induced changes in soil carbon pools. *Biogeosciences* **10**, 2393–2407 (2013).
- Sprovieri, F. *et al.* Atmospheric mercury concentrations observed at ground-based monitoring sites globally distributed in the framework of the GMOS network. *Atmos. Chem. Phys.* **16**, 11915–11935 (2016).

**Supplementary Information** is available in the online version of the paper.

**Acknowledgements** We thank Toolik Field Station and Polar Field Services staff for their support in setting up the field site and maintaining its operation for two years, with special thanks to J. Timm. We thank O. Dillon and C. Pearson for support with laboratory analyses; A. Steffen and S. Brooks for providing additional instrumentation; J. Chmieleff for support with inductively coupled plasma mass spectrometry; and R. Kreidberg and J. Arnone for editorial and technical assistance in manuscript preparation. The project was funded primarily by a US National Science Foundation (NSF) award (PLR 1304305), with additional support provided by further NSF (CHN 1313755) and US Department of Energy (DE-SC0014275) awards. The Hg isotope work was funded by H2020 Marie Skłodowska-Curie grant agreement no. 657195 to M.J., and European Research Council grant ERC-2010-StG\_20091028 and CNRS-INSU-CAF funding (PARCS project) to J.E.S.

**Author Contributions** D.O. and D.H. initiated and designed this project, and M.J., J.E.S. and D.O. designed and developed the isotope component. All authors were involved in all field sampling and/or laboratory analyses. Y.A. led data analysis of flux data, and M.J. led stable isotope sampling and analysis with support from J.E.S. D.O. led manuscript writing with major support from M.J., Y.A., J.E.S. and C.W.M.

**Author Information** Reprints and permissions information is available at [www.nature.com/reprints](http://www.nature.com/reprints). The authors declare no competing financial interests. Readers are welcome to comment on the online version of the paper. Publisher's note: Springer Nature remains neutral with regard to jurisdictional claims in published maps and institutional affiliations. Correspondence and requests for materials should be addressed to D.O. (Daniel\_Obrist@uml.edu).

**Reviewer Information** *Nature* thanks J. Blum and the other anonymous reviewer(s) for their contribution to the peer review of this work.

## METHODS

**The study site.** The study site is located near Toolik Field Station (68° 38' N, 149° 36' W), a research station operated by the University of Alaska, Fairbanks. All measurement systems were located in a tussock tundra, with underlying soil types characterized as typical aquiturbels, with active layer depths between 60 cm and 100 cm. All analysers and control systems were housed in a temperature-controlled field laboratory (Extended Data Fig. 1) built on the tundra, and sampling lines and sensors were routed outside to the tundra sampling locations via heated conduits. This set-up allowed year-round measurements of trace-gas dynamics, including throughout the Arctic winter, without damage from icing, animal disturbances, or other issues.

**Overview of key measurements.** During two full years, we measured continuous net surface–atmosphere fluxes of gaseous Hg(0) (that is, the balance of deposition and volatilization); to our knowledge such measurements have previously been conducted year-round only in two temperate grassland sites<sup>31,32</sup>. Campaign-style wet deposition measurements composed of Hg(II) species<sup>33</sup> were conducted approximately every six weeks throughout the two years, and included snowfall and rain measurements, surface snow and full snowpack collection, and subsequent analysis of total dissolved Hg after melting. Hg(II) dry deposition was assessed by pyrolyzer measurements (see below) to quantify atmospheric Hg(II) concentrations multiplied by deposition velocity. Hg(II) dry deposition measurements were conducted only from the middle of February through to the middle of September 2016, but we used auxiliary Arctic studies to constrain mid-winter patterns<sup>1,34</sup> (see below and Supplementary Information). In addition, we measured gaseous Hg(0) in interstitial air of snowpack and tundra soils at multiple locations and depths in the tundra during two full years, to assess atmosphere–snow–soil diffusion profiles and to pinpoint active source and sink zones of Hg(0). For this, a snow tower (Extended Data Fig. 1; refs 35, 36) was deployed to measure Hg(0) gas concentrations in interstitial snow pores at multiple depths in the undisturbed tundra snowpack. In addition, a soil trace-gas system (Extended Data Fig. 1; ref. 25) consisting of six gas wells provided gaseous Hg(0) concentrations in soil pores at three depths each in two tundra soil profiles. During summers, field campaigns were conducted for detailed characterization of concentrations and pool sizes of Hg in all major ecosystem matrices, including vegetation as well as organic and mineral soil layers. Characterization of Hg stable isotope compositions were conducted in snow, soils, plants, and the atmosphere to complement source and sink processes of Hg in this tundra ecosystem.

**Micrometeorological flux measurements.** To quantify gaseous Hg(0) exchange at the ecosystem level, we used an aerodynamic flux method (Extended Data Fig. 1). Surface–atmosphere flux was calculated by measuring concentration gradients in the atmosphere above the tundra in conjunction with atmospheric turbulence parameters, as follows:

$$F_{\text{Hg}(0)} = -\frac{k \times u_* \times z}{\phi_h(z/L)} \times \frac{\partial c(\text{Hg}(0))}{\partial z}$$

where  $k$  denotes the von Karman constant (0.4);  $u_*$  is the friction velocity;  $z$  is the measurement height;  $\phi_h(z/L)$  is the universal temperature profile;  $L$  is the Monin–Obukhov length; and  $\partial c(\text{Hg}(0))/\partial z$  is the vertical Hg(0) gas concentration gradient. Hg(0) concentrations at heights of 61 cm and 363 cm above the soil surface were measured through 0.2  $\mu\text{m}$  Teflon inlet filters connected to perfluoroalkoxy (PFA) lines, a setup that measures gaseous Hg(0) (ref. 37). A valve control system with three-way solenoid valves (NResearch, West Caldwell, New Jersey, USA) allowed switching between the gradient inlets every 10 min. Solenoids were connected to a set of trace-gas analysers with a total sampling flow of 1.51  $\text{min}^{-1}$ . This system included: an air mercury analyser (model 2537A, Tekran, Toronto, Canada); a cavity ring-down (CRD) greenhouse-gas analyser to measure  $\text{CO}_2$ ,  $\text{H}_2\text{O}$ , and  $\text{CH}_4$  (Los Gatos Research, San Jose, USA); an  $\text{O}_3$  analyser (model 491, Thermo Scientific, Waltham, USA); and an  $\text{O}_2$  analyser (Model 1440, Servomex, East Sussex, UK).

Fluxes were calculated only during periods of appropriate turbulence according to ref. 38, and periods when  $z/L$  was less than  $-0.2$  and more than  $0.2$  were removed from the data set. The tundra measurement site was bordered by Toolik Lake to the north, and we removed data when flux footprints originated from Toolik Lake or its edge ( $0^\circ$ – $40^\circ$  and  $300^\circ$ – $360^\circ$ ; 27% of the data). For gap-filling of periods when measurements were missing, or when fluxes originated from the nearby lake, or when conditions did not fulfil the criteria for acceptable turbulence to calculate fluxes, we interpolated flux data using the average diel pattern of each respective month. For quality control, sampling lines were confirmed to be free of contamination during each field visit (approximately every six weeks, using Hg-free air; model 1100, Tekran). In addition, line intercomparisons were conducted at the same intervals to test for line biases between the upper and lower inlet lines; for this, both upper and lower inlet lines were set at the same height and measurements

were conducted to assess offset. Line intercomparison tests showed no substantial line offsets throughout the study, with the exception of one time when a leak was detected and immediately fixed, and fluxes before that time were corrected.

**Snow tower.** Next to the flux tower (approximately 2 m away), we deployed a snow tower (Extended Data Fig. 1) to measure gaseous Hg(0) and auxiliary trace-gas concentrations in the undisturbed snowpack at multiple heights. The snow tower<sup>35,36</sup> consists of vertical square aluminium bars with 60-cm crossarms at five heights that hold a total of ten sampling inlets. The horizontal crossbars that support air inlets were set at heights of 0 cm, 10 cm, 20 cm, 30 cm and 110 cm above the soil surface, with the lower four inlets generally buried in snow for most of the winter to measure snow pore air; the uppermost inlet was always located above the snowpack and measured atmospheric Hg(0) gas concentrations. Each crossbar supported a pair of connected air inlets, spaced 60 cm apart, and fitted with 25 mm syringe filters with 1  $\mu\text{m}$  glass-fibre membranes (Pall Life Sciences, Ann Arbor, Michigan, USA) connected to PFA lines. The snow-tower lines were connected to a Teflon valve control box and data-acquisition system inside the heated laboratory. These lines were further connected to a second set of trace-gas analysers, including for gaseous Hg(0) and ozone (models as above), and for  $\text{CO}_2$  and  $\text{H}_2\text{O}$  (model LI840A, LI-COR, Lincoln, USA). Sampling flow rates were set between 2.71  $\text{min}^{-1}$  and 3.01  $\text{min}^{-1}$ , and the sampling sequence was set to extract snow air at each height for 10-min measurement periods, so that a full sequence of all five inlet heights was sampled every 50 min. Measurements of ambient air gaseous Hg(0) concentrations measured at the top inlet of the snow-tower system compared well with ambient air Hg(0) concentrations measured by the micrometeorological tower.

**A soil trace-gas measurement system.** We used a system similar to that described in ref. 25 (Extended Data Fig. 1) to allow monitoring of soil pore trace gases at multiple depths and locations. In the first year, the soil trace-gas system consisted of six Teflon wells (63.5 cm length, 10.2 cm diameter) with inside volumes of 4.2 litres. One side of each well was perforated with 65 holes of 0.64 cm diameter, for a total perforated area of 20.6  $\text{cm}^2$ . The holes were covered with Gore-Tex membranes and Teflon screens, both of which were held in place by stainless-steel brackets and pipe clamps to produce a watertight seal, allowing gas diffusion into the wells while keeping out soil water. The soil wells were placed at two tundra soil profiles (at depths of 10 cm, 20 cm and 40 cm); one profile consisted mainly of organic soil layers and a second mainly of mineral horizons. The six wells were connected by PFA lines to the heated laboratory and connected to the same instrumentation set to measure trace-gas gradients for flux measurements (gaseous Hg(0),  $\text{CO}_2$ ,  $\text{H}_2\text{O}$ ,  $\text{CH}_4$ ,  $\text{O}_3$ , and  $\text{O}_2$ ). The system, operated at a flow rate of 1.51  $\text{min}^{-1}$ , was programmed to extract a sequence of soil measurements (for 10 min each) only three times per day to reduce the air volume extracted from the soil profile and to minimize disturbance and advection effects. Because of water intrusion into the soil gas wells in June 2015, the system was replaced with a different system consisting of 47 mm Teflon inlet filters with additional inlet holes drilled at the bottom of the filters and mounted upside down in the soil profile at the same six locations. Testing in saturated water showed that the hydrophobic Teflon filters prevented water intrusion into the sampling lines using this inlet configuration. Both soil trace-gas systems were extensively tested in Hg-free air and ambient air before deployment to confirm that they were free of contamination. These systems showed quick equilibrium with ambient air Hg(0) concentrations, and there was no memory effect when switching the sampling lines. Both measurement systems provided the same magnitude and seasonal patterns of gaseous Hg(0) soil concentrations (Fig. 3).

**Atmospheric Hg(II) concentrations.** We measured atmospheric Hg(II) concentrations by using a third gaseous mercury analyser (model 2537; Tekran) in conjunction with a pyrolyzer unit. Hg(II) concentrations were calculated by differential measurements of air drawn from an inlet configured to measure gaseous Hg(0) (using 0.2  $\mu\text{m}$  Teflon inlet filters) and a second inlet stream without a filter routed through a pyrolyzer oven set at 650  $^\circ\text{C}$ , whereby all atmospheric Hg forms were converted into gaseous Hg(0) (to measure total Hg). A valve-switching unit (model 1110, Tekran) was used to alternate measurements between total Hg and gaseous Hg(0) measurements every 10 min, and allowed Hg(II) concentrations to be calculated by difference (similar to the method described in ref. 39). To make a pyrolyzer oven, we modified a particulate mercury speciation module (model 1135; Tekran) and used a quartz tube filled with quartz chips as a pyrolyzer inlet that directly reached the ambient atmosphere for sampling. In addition, the particulate filter inside the glassware was removed, and the quartz tube was filled with quartz chips to increase the surface area and serve as an efficient catalyst. The detection limit of this system, based on a three times standard deviation of the blanks, was 33  $\text{pg m}^{-3}$ .

The pyrolyzer unit was deployed from the middle of February to the middle of September 2016 (Extended Data Fig. 2). Atmospheric Hg(II) concentration measurements were lacking from October through to mid-February, but we

found undetectable levels (less than  $0.033 \text{ ng m}^{-3}$ ) or low levels (generally less than  $0.05 \text{ ng m}^{-3}$ ) in other winter months, similar to the low or undetectable concentrations detected outside of AMDE periods at other Arctic locations<sup>34</sup>. For 2015, we assumed similar Hg(II) concentrations to those measured in 2016. Negative numbers in the Hg(II) record represent noise levels of differential measurements as well as data produced during strong fluctuations of total atmospheric Hg concentrations (that is, during AMDE depletion recoveries). We calculated the atmospheric deposition of Hg(II) to be  $2.5 \mu\text{g m}^{-2} \text{ yr}^{-1}$  by multiplying measured Hg(II) concentrations by a proposed Hg(II) deposition velocity of  $1.5 \text{ cm s}^{-1}$  over various surfaces<sup>40</sup>, the range of atmospheric Hg(II) deposition was  $0.8\text{--}2.8 \mu\text{g m}^{-2} \text{ yr}^{-1}$  (based on deposition velocities of generally between  $0.5 \text{ cm s}^{-1}$  and  $1.7 \text{ cm s}^{-1}$ )<sup>40</sup>. Even lower annual atmospheric Hg(II) deposition ( $0.1 \mu\text{g m}^{-2}$ ) has been independently estimated for this area on the basis of nearby Arctic lake studies<sup>1</sup>. Low wintertime Hg(II) concentrations and deposition are furthermore consistent with extremely low wintertime snowfall Hg concentrations (these are, on average,  $0.26 \text{ ng l}^{-1}$ ; Supplementary Table 2), which are derived from Hg(II) scavenged from the atmosphere. Finally, Hg stable isotope signatures are consistent with low amounts of Hg(II) deposition measured at this site.

**Atmospheric wet deposition of Hg and snow Hg(II).** We characterized the wet deposition of Hg (mainly Hg(II)) and snow Hg(II) through frequent collection of surface snow and manual collection of rainfall using trace-metal collection techniques (gloves, acid-cleaned Teflon and stainless-steel sampling equipment). Samples were analysed for Hg concentrations after filtering through filters of pore size  $0.45 \mu\text{m}$ . A total of 19 sampling dates was used for calculation of wet deposition loads (Supplementary Table 2). Surface snow samples (top 3 cm) were transferred directly into new, sterile polyethylene sampling bags (whirl-pak bags; Nasco, Fort Atkinson, Wisconsin, USA). Fresh snow was taken directly from the surface into the sampling bags; additional snowpack sampling was performed from the top to the bottom of the snowpack using acid-cleaned stainless-steel cutters (Model RIP 1 1000 cc cutter; Snowmetrics, Fort Collins, Colorado, USA). In addition, snowpack sampling was performed on five dates, using two excavated snow pits each, which were sampled using a stainless-steel snow cutter (RIP 1 cutter 1000 cc) and then transferred directly to the sterile polyethylene sampling bags (double bags). Each snow pit was sampled at ten centimetre-layer increments from the top to the bottom of the snow pit. Per layer, two replicate samples from perpendicular walls of the pit were pooled together for analysis. Summertime collection of rainwater was performed manually using an acid-cleaned Teflon funnel and Teflon bottles.

We determined total dissolved Hg according to US Environmental Protection Agency (EPA) method 1,631 for total mercury in water, using dual-stage gold pre-concentration and an Hg water analyser (model 2600; Tekran). Annual atmospheric wet deposition was calculated using volumetric precipitation measured at Toolik Field Station, multiplied by respective snow and rain Hg concentrations (Supplementary Table 2).  $\text{Hg}_{\text{tot}}$  and  $\text{Hg}_{\text{diss}}$  concentrations were determined by cold-vapour atomic fluorescence spectrometry (Tekran 2600 spectrometer), using bromine monochloride and hydroxylamine hydrochloride digestion according to EPA method 1,631. The detection limits, determined as three times the standard deviation of blank samples, averaged  $0.08 \text{ ng l}^{-1}$ . Recoveries, as determined by  $5 \text{ ng l}^{-1}$  standards analysed after every ten samples, averaged between 93% and 107%. Laboratory and field blanks were conducted for both the stainless-steel-cutter method (using water rinses) and the whirl-pak-bag method for snow sampling, and both showed no metal contamination (all blank determinations are below detection limits).

**Soil and vegetation Hg concentrations.** We determined soil and vegetation Hg concentrations from samples collected during multiple field sampling campaigns, from spring through to the end of autumn of 2014, 2015 and 2016. All samples were freeze-dried, milled, and analysed according to US EPA method 7,473 using a total mercury analyser (model MA-2000; Nippon, Takatsuki, Japan) and as described in detail in ref. 26. To estimate annual Hg uptake by vegetation and standing aboveground biomass pools (Supplementary Table 4), we used data on vegetation dynamics (aboveground net primary productivity (NPP) and aboveground vegetation biomass) from refs 41, 42.

**Hg stable isotope measurements.** We carried out Hg stable isotope measurements (Extended Data Figs 4, 5 and Extended Data Tables 1–5) on Hg extracted from subsamples of dried and milled vegetation, soil, and rock samples using a two-step oven combustion system<sup>21</sup>. Snow samples were processed using a purge-and-trap system<sup>23</sup>, which was scaled up to 20-litre bottles to attain Hg amounts that were large enough from snow samples with low Hg concentrations. Sample blanks, recoveries, and Hg isotopic compositions of processing standards (mercury standard solution NIST-3133) were analysed (Extended Data Table 4). Atmospheric gaseous Hg(0) was collected continuously from a separate inlet at the flux tower, equipped with a glass-fibre filter (as described for snow-tower measurements) and

a heated PFA line to the field laboratory. Atmospheric gaseous Hg(0) (typically sampled at 0.21 per minute for periods of 6–8 weeks) was collected on iodated activated carbon traps (IC traps, 125 mg), which were processed using a combustion method adapted from ref. 43. Gaseous Hg(0) breakthrough from IC traps was measured regularly during the sampling campaign using a Tekran 2537 mercury analyser, and was always below the detection limit ( $0.05 \text{ ng m}^{-3}$ ). Procedural blanks, procedural standards, and sample recoveries were measured for quality assurance (Extended Data Table 1). Hg isotopic ratios were measured by cold-vapour multi-collector inductively coupled plasma mass spectrometry (CV-MC-ICPMS; Neptune, Thermo-Finnigan, Germany) at the Midi-Pyrenees Observatory (Toulouse, France), using measurement protocols described elsewhere<sup>20,43</sup>.

Hg isotopic signatures are expressed using the common nomenclature of 'small delta' notation for mass-dependent fractionation signatures (MDFs):

$$\delta^{\text{xxx}}\text{Hg}_{\text{NIST-3133}} = \left( \frac{(\text{xxxHg}/^{198}\text{Hg})_{\text{Sample}}}{(\text{xxxHg}/^{198}\text{Hg})_{\text{NIST-3133}}} - 1 \right) \times 10^3$$

where xxx corresponds to masses 199, 200, 201, 202 and 204. Mass-independent Hg isotopic fractionation signatures (MIFs) are expressed by 'capital delta' notation:

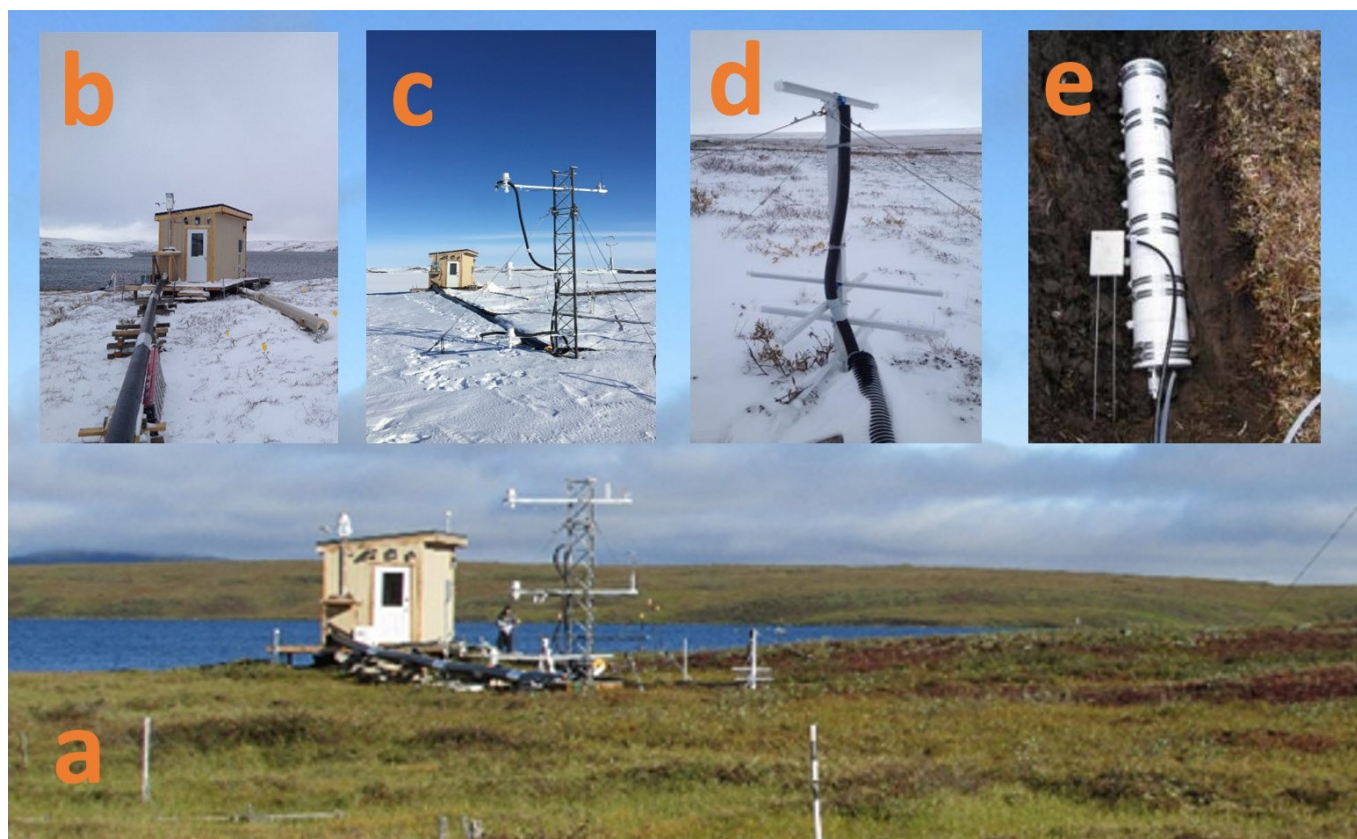
$$\Delta^{\text{yyy}}\text{Hg} = \delta^{\text{yyy}}\text{Hg} - (\delta^{202}\text{Hg} \times \text{s.f.})$$

where yyy corresponds to masses 199, 200, 201 and 204; and s.f. to the kinetic mass-dependent scaling factors 0.2520, 0.5024, 0.7520 and 1.493, for  $\Delta^{199}\text{Hg}$ ,  $\Delta^{200}\text{Hg}$ ,  $\Delta^{201}\text{Hg}$  and  $\Delta^{204}\text{Hg}$ , respectively. Analytical precision and accuracy were assured through repetitive measurements of in-house standards for ETH-Fluka ( $\delta^{202}\text{Hg} = -1.43 \pm 0.19\text{‰}$ ,  $\Delta^{199}\text{Hg} = 0.08 \pm 0.07\text{‰}$ ,  $\Delta^{200}\text{Hg} = 0.02 \pm 0.07\text{‰}$ ; 2 s.d.;  $n = 38$ ) and for UM-Almaden ( $\delta^{202}\text{Hg} = -0.56 \pm 0.10\text{‰}$ ,  $\Delta^{199}\text{Hg} = -0.02 \pm 0.06\text{‰}$ ,  $\Delta^{200}\text{Hg} = 0.01 \pm 0.07\text{‰}$ ; 2 s.d.  $n = 9$ ); these standards were in agreement with previously reported values<sup>19–21</sup>.

**Data availability.** The Hg concentration data from plants, soils, precipitation and snowpack generated during this study are included in the Extended Data Tables and Supplementary Information. Stable isotope data are provided in Extended Data and in Supplementary Information. Metadata and snow, soil chemical, and atmospheric data will be archived at the NSF Arctic Data Centre (<https://arcticdata.io>). Additional information and/or higher-resolution data sets are available from the corresponding author on request.

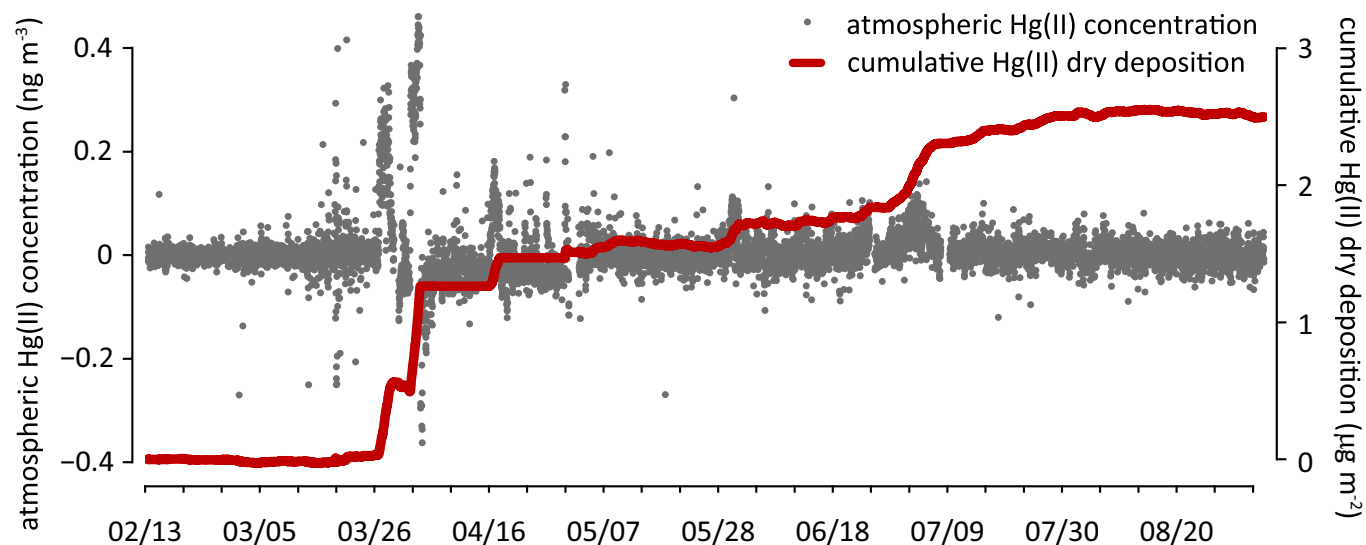
1. Fritzsche, J. *et al.* Elemental mercury fluxes over a sub-alpine grassland determined with two micrometeorological methods. *Atmos. Environ.* **42**, 2922–2933 (2008).
2. Castro, M. & Moore, C. Importance of gaseous elemental mercury fluxes in western Maryland. *Atmosphere* **7**, 110 (2016).
3. Douglas, T. A. *et al.* Influence of snow and ice crystal formation and accumulation on mercury deposition to the Arctic. *Environ. Sci. Technol.* **42**, 1542–1551 (2008).
4. Cole, A. S. *et al.* Ten-year trends of atmospheric mercury in the high Arctic compared to Canadian sub-Arctic and mid-latitude sites. *Atmos. Chem. Phys.* **13**, 1535 (2013).
5. Seok, B. *et al.* An automated system for continuous measurements of trace gas fluxes through snow: an evaluation of the gas diffusion method at a subalpine forest site, Niwot Ridge, Colorado. *Biogeochemistry* **95**, 95–113 (2009).
6. Fain, X. *et al.* Mercury dynamics in the Rocky Mountain, Colorado, snowpack. *Biogeosciences* **10**, 3793–3807 (2013).
7. Moore, C. W., Obrist, D. & Luria, M. Atmospheric mercury depletion events at the Dead Sea: spatial and temporal aspects. *Atmos. Environ.* **69**, 231–239 (2013).
8. Edwards, G. C. *et al.* Development and evaluation of a sampling system to determine gaseous mercury fluxes using an aerodynamic micrometeorological gradient method. *J. Geophys. Res.* **110**, D10306 (2005).
9. Lyman, S. N. & Jaffe, D. A. Formation and fate of oxidized mercury in the upper troposphere and lower stratosphere. *Nat. Geosci.* **5**, 114–117 (2012).
10. Zhang, L., Wright, L. P. & Blanchard, P. A review of current knowledge concerning dry deposition of atmospheric mercury. *Atmos. Environ.* **43**, 5853–5864 (2009).
11. Shaver, G. R. & Chapin, F. S. Production: biomass relationships and element cycling in contrasting Arctic vegetation types. *Ecol. Monogr.* **61**, 1–31 (1991).
12. Chapin, F. S., Shaver, G. R., Giblin, A. E., Nadelhoffer, K. J. & Laundre, J. A. Responses of Arctic tundra to experimental and observed changes in climate. *Ecology* **76**, 694–711 (1995).
13. Fu, X., Heimbürger, L.-E. & Sonke, J. E. Collection of atmospheric gaseous mercury for stable isotope analysis using iodine- and chlorine-impregnated activated carbon traps. *J. Anal. At. Spectrom.* **29**, 841–852 (2014).
14. Bergquist, B. A. & Blum, J. D. Mass-dependent and -independent fractionation of Hg isotopes by photoreduction in aquatic systems. *Science* **318**, 417–420 (2007).





**Extended Data Figure 1 | Research site and measurement systems used in this study.** **a**, The research site was characterized as Tussock tundra, and is located at Toolik Field Station in northern Alaska, USA ( $68^{\circ} 38' \text{ N}$ ,  $149^{\circ} 36' \text{ W}$ ). **b**, A temperature-controlled research laboratory was set up to house analytical sensors, control systems, and data acquisition. Heated conduits were installed to run electrical lines and trace-gas lines to the tundra and to protect lines from bite damage and freezing. **c**, Continuous gaseous  $\text{Hg}(0)$  flux measurements were conducted using an aerodynamic method based on gradient measurements at heights of 61 cm and 363 cm above ground. **d**, A snow tower, consisting of five trace-gas inlets, was

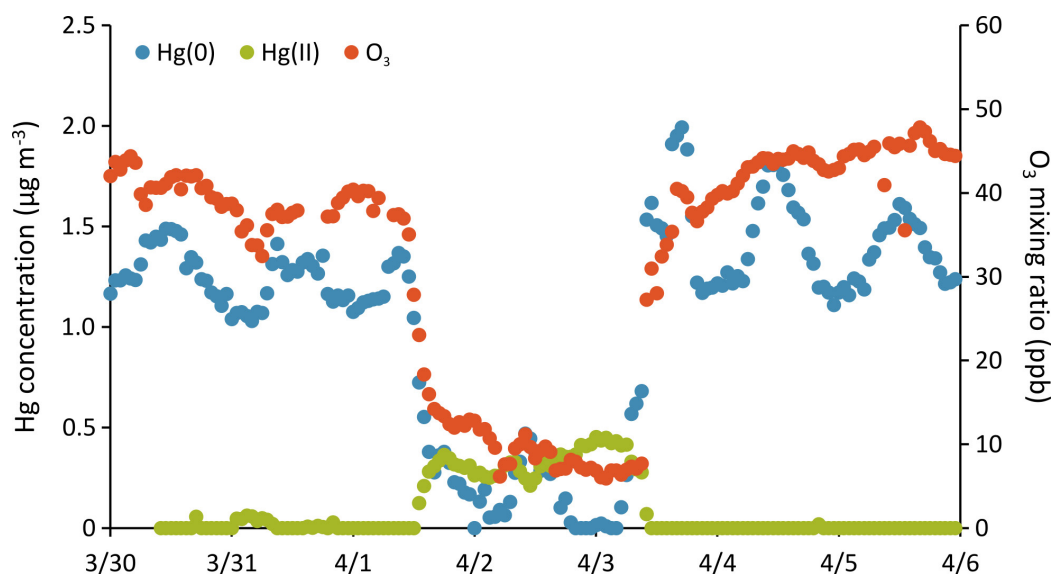
established over the tundra before the onset of snowfall. Wintertime snowfall buried this tower and allowed sampling of snow air from the respective air inlets without disturbing the snowpack. **e**, A soil trace-gas system, consisting of six trace-gas wells at various depths and locations, was deployed in tundra soils to allow three daily extractions of soil pore gas and analysis for  $\text{Hg}(0)$  gas and auxiliary trace gases. Panel **e** shows an example of the wells used in year one; these were replaced with a different system in year two but detected similar gas magnitudes and seasonal patterns.



**Extended Data Figure 2 | Measured atmospheric Hg(II) concentrations from February to September 2016, and estimated Hg(II) dry deposition.** Hg(II) concentrations were measured by using differential measurements of gaseous Hg(0) and total atmospheric Hg, which passed through a

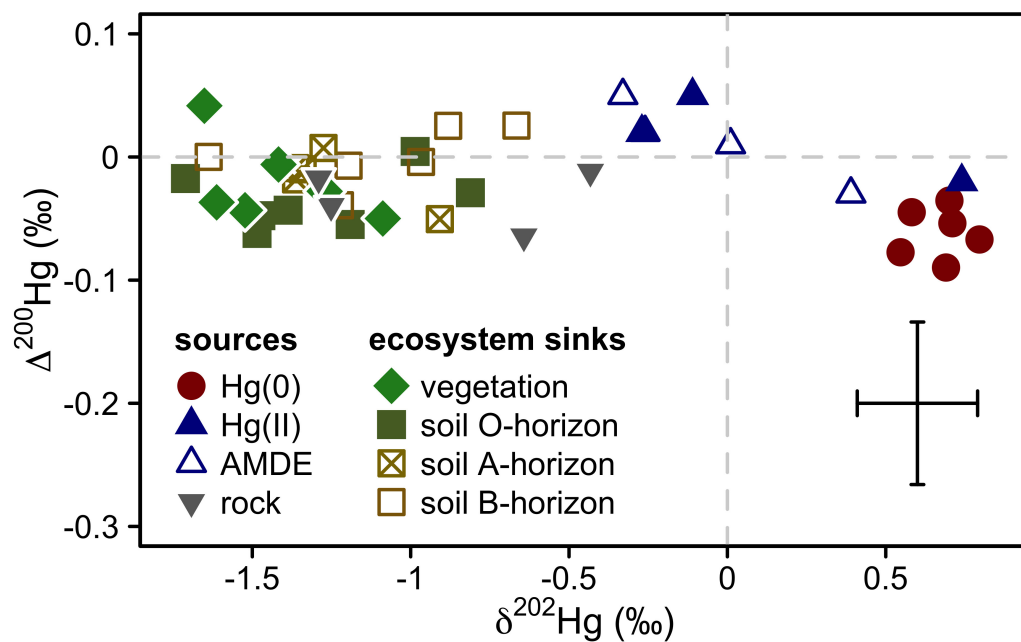
glass-tube inlet directly into a pyrolyzer oven set at  $650^\circ\text{C}$ . Cumulative Hg(II) deposition was calculated on the basis of reported deposition velocities for Hg(II) forms of  $1.5 \text{ cm s}^{-1}$ .





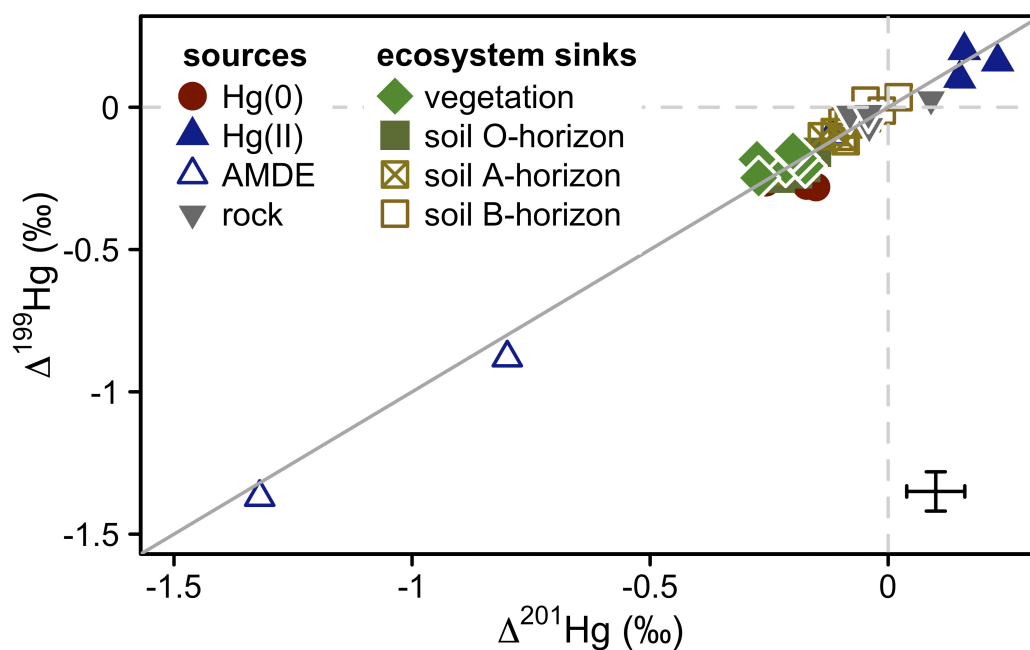
**Extended Data Figure 3 | Example of a springtime AMDE at Toolik Field Station, from 1–3 April 2016.** This atmospheric Hg measurement sequence shows corresponding concentration depletions of Hg(0) (in blue) and O<sub>3</sub> (in red), along with the formation of atmospheric Hg(II)

(in green). Hg(0) concentrations reached values below the detection limit when Hg(II) concentrations increased to 0.5 ng m<sup>-3</sup>. At the same time, O<sub>3</sub> mixing ratios dropped down from 45 ppb to less than 10 ppb.



**Extended Data Figure 4 | Mass-independent anomalies of even-mass-number Hg isotopes ( $\Delta^{200}\text{Hg}$ ) and mass-dependent Hg isotopic signatures ( $\delta^{202}\text{Hg}$ ) for different Hg sources and ecosystem sinks.** Symbols for sources include: circles for atmospheric Hg(0); filled blue triangles for Hg(II) in snow deposited before January/February 2016; open blue triangles for Hg measured in surface snow during periods of AMDEs (March/April 2016); and grey inverted triangles for geogenic Hg in

bedrock samples. Symbols for tundra components include: filled diamonds for bulk vegetation; filled squares for organic (O horizon) soils; and open squares with a cross for mineral soil A horizons (which have more than 10% organic matter) or without cross for B horizons (which have less than 10% organic matter). Measurement uncertainties, calculated as 2 s.d. of replicate standards, are shown on the lower right.



**Extended Data Figure 5 | Mass-independent Hg isotopic anomalies ( $\Delta^{199}\text{Hg}$  and  $\Delta^{201}\text{Hg}$ ) for different Hg sources and ecosystem sinks.** Symbols for sources include: circles for atmospheric Hg(0); filled blue triangles for Hg(II) in snow deposited before January/February 2016; open blue triangles for Hg deposited during AMDEs (March/April 2016); and grey inverted triangles for geogenic Hg in bedrock samples. Symbols for tundra components include: filled diamonds for bulk vegetation; filled squares for organic (O horizon) soils; and open squares with a cross

for mineral soil A horizons (more than 10% organic matter) or without a cross for B horizons (less than 10% organic matter). Measurement uncertainties, calculated as 2 s.d. of replicate standards, are shown on the lower right. All data are within analytical uncertainty, with the straight line representing the 1:1  $\Delta^{199}\text{Hg}$  to  $\Delta^{201}\text{Hg}$  slope, thought to be representative of photochemically induced mass-independent fractionation by magnetic isotope effects<sup>44</sup>.



Extended Data Table 1 | Hg stable isotope compositions of atmospheric gaseous Hg(0) collected on iodated carbon traps

name	start	end	flow	volume	amount	yield	n	$\delta^{204}\text{Hg}$	$\delta^{202}\text{Hg}$	$\delta^{201}\text{Hg}$	$\delta^{200}\text{Hg}$	$\delta^{199}\text{Hg}$	$\Delta^{204}\text{Hg}$	$\Delta^{201}\text{Hg}$	$\Delta^{200}\text{Hg}$	$\Delta^{199}\text{Hg}$
Samples			(L min <sup>-1</sup> )	(m <sup>3</sup> )	(ng)	(%)		(‰)	(‰)	(‰)	(‰)	(‰)	(‰)	(‰)	(‰)	(‰)
GEM_P1-C	17.08.15	14.10.15	0.195	16.1	22.3	126	3	1.09	0.71	0.31	0.30	-0.05	0.03	-0.22	-0.05	-0.23
GEM_P1-D	17.08.15	14.10.15	0.185	15.3	13.1	78	2	1.01	0.70	0.32	0.32	-0.01	-0.04	-0.21	-0.04	-0.19
GEM_P2-D	20.10.15	04.12.15	0.197	12.7	11.2	86	1	0.96	0.55	0.20	0.20	-0.10	0.15	-0.21	-0.08	-0.23
GEM_P3-C	08.12.15	27.01.16	0.199	14.3	18.3	114	1	1.07	0.58	0.18	0.25	-0.12	0.20	-0.26	-0.04	-0.26
GEM_P4-C	02.02.16	23.03.16	0.173	11	13.7	93	2	1.24	0.69	0.35	0.26	-0.10	0.21	-0.17	-0.09	-0.28
GEM_P4-D	02.02.16	23.03.16	0.193	12.3	20.6	125	1	1.17	0.80	0.45	0.33	-0.08	-0.02	-0.15	-0.07	-0.28
<b>Standards</b>																
NIST					13.3	133	2	0.06	0.04	0.02	0.02	0.00	-0.01	-0.01	0.00	-0.01
Hg0-vapor inj. 1					6.4	89	1	-1.77	-1.37	-1.03	-0.68	-0.09	0.28	0.00	0.01	0.26
Hg0-vapor inj. 2					8.8	123	2	-2.21	-1.60	-1.12	-0.79	-0.26	0.19	0.09	0.02	0.14
Hg0-vapor direct 1							1	-2.64	-1.68	-1.24	-0.83	-0.34	-0.12	0.02	0.01	0.08
Hg0-vapor direct 2							1	-2.47	-1.58	-1.10	-0.72	-0.30	-0.10	0.09	0.08	0.10
Hg0-vapor direct 3							1	-2.34	-1.44	-1.03	-0.75	-0.26	-0.18	0.05	-0.03	0.10

The table includes: the sample name; the start and end date of sampling; the flow rate (in litres per minutes); the volume of air collected; the amount of Hg collected on the trap; the sample yield; the number of analyses (*n*); and the mean Hg isotope compositions of samples and procedural standards (as standards, we used NIST-3133, as well as saturated Hg(0) gas injected onto the iodated carbon trap). Procedural blanks were below the analytical detection limit (0.75 ng, *n* = 3).

Extended Data Table 2 | Hg isotope compositions of vegetation

name	n	$\delta^{204}\text{Hg}$ (‰)	$\delta^{202}\text{Hg}$ (‰)	$\delta^{201}\text{Hg}$ (‰)	$\delta^{200}\text{Hg}$ (‰)	$\delta^{199}\text{Hg}$ (‰)	$\Delta^{204}\text{Hg}$ (‰)	$\Delta^{201}\text{Hg}$ (‰)	$\Delta^{200}\text{Hg}$ (‰)	$\Delta^{199}\text{Hg}$ (‰)
Bulkveg-P2	2	-1.58	-1.09	-0.99	-0.60	-0.48	0.05	-0.17	-0.05	-0.21
Bulkveg-pooled-a	3	-2.25	-1.52	-1.36	-0.81	-0.59	0.03	-0.22	-0.04	-0.20
Bulkveg-pooled-b	3	-2.18	-1.42	-1.34	-0.72	-0.54	-0.06	-0.28	-0.01	-0.18
Bulkveg-P4	2	-2.42	-1.61	-1.40	-0.85	-0.59	-0.01	-0.19	-0.04	-0.18
Bulkveg-3/4	2	-2.43	-1.65	-1.44	-0.79	-0.57	0.03	-0.20	0.04	-0.15
Bulkveg-1/4	1	-1.83	-1.27	-1.23	-0.67	-0.57	0.07	-0.27	-0.03	-0.25

The table shows: the sample name; the number of analyses (*n*); and Hg isotopic signatures of bulk vegetation samples.

Extended Data Table 3 | Hg stable isotope compositions of soil and rock (geogenic) samples

name	horizon	n	$\delta^{204}\text{Hg}$ (‰)	$\delta^{202}\text{Hg}$ (‰)	$\delta^{201}\text{Hg}$ (‰)	$\delta^{200}\text{Hg}$ (‰)	$\delta^{199}\text{Hg}$ (‰)	$\Delta^{204}\text{Hg}$ (‰)	$\Delta^{201}\text{Hg}$ (‰)	$\Delta^{200}\text{Hg}$ (‰)	$\Delta^{199}\text{Hg}$ (‰)
<b>Samples</b>											
P5-Oe	O	2	-1.42	-0.99	-0.91	-0.49	-0.45	0.05	-0.17	0.00	-0.20
P5-Oe	O	2	-1.19	-0.81	-0.83	-0.44	-0.41	0.03	-0.22	-0.03	-0.21
P6-Oe/a	O	2	-2.18	-1.49	-1.31	-0.81	-0.61	0.04	-0.19	-0.06	-0.23
P7-Oe	O	2	-1.72	-1.19	-1.13	-0.65	-0.54	0.05	-0.24	-0.05	-0.24
P7-Oa_upper	O	3	-2.18	-1.47	-1.33	-0.79	-0.62	0.02	-0.23	-0.05	-0.25
P7-Oa_lower	O	3	-2.05	-1.39	-1.22	-0.74	-0.56	0.03	-0.17	-0.04	-0.21
P8-Oa_lower	O	2	-2.47	-1.71	-1.44	-0.88	-0.59	0.08	-0.15	-0.02	-0.16
P2_Oa	O	1	-1.24	-0.91	-0.82	-0.51	-0.33	0.11	-0.14	-0.05	-0.10
P5-A	A	2	-2.03	-1.36	-1.27	-0.70	-0.57	0.00	-0.25	-0.02	-0.23
P6-A	A	2	-1.95	-1.34	-1.10	-0.68	-0.46	0.05	-0.09	-0.01	-0.12
P7-A-25+	A	2	-2.03	-1.36	-1.14	-0.69	-0.43	0.00	-0.11	-0.01	-0.09
P8-A-27+	A	2	-1.88	-1.28	-1.04	-0.63	-0.38	0.02	-0.08	0.01	-0.06
P5-E	B	3	-1.80	-1.22	-1.02	-0.65	-0.36	0.02	-0.10	-0.04	-0.05
P6-B_upper	B	3	-1.46	-0.97	-0.82	-0.49	-0.35	-0.01	-0.10	0.00	-0.10
P6-B_lowerr	B	4	-1.83	-1.20	-0.91	-0.61	-0.31	-0.04	-0.01	-0.01	-0.01
P2-B_upper	B	1	-2.34	-1.64	-1.21	-0.82	-0.38	0.11	0.02	0.00	0.04
P2-B_middle	B	1	-1.32	-0.88	-0.71	-0.42	-0.20	0.00	-0.05	0.03	0.02
P2-B_lower	B	1	-1.03	-0.67	-0.55	-0.31	-0.21	-0.04	-0.04	0.03	-0.04
P3_rock	rock	2	-1.06	-0.64	-0.52	-0.39	-0.23	-0.10	-0.04	-0.06	-0.07
Rock_1/3	rock	1	-0.63	-0.43	-0.41	-0.23	-0.13	0.02	-0.08	-0.01	-0.02
Rock_2/3	rock	1	-1.73	-1.25	-0.85	-0.67	-0.29	0.14	0.09	-0.04	0.03
Rock_3/3	rock	1	-2.00	-1.29	-1.01	-0.67	-0.35	-0.08	-0.04	-0.02	-0.02
<b>Standards</b>											
BCR-482		2	-2.39	-1.56	-1.85	-0.72	-1.04	-0.06	-0.68	0.06	-0.65
MESS3		3	-2.80	-1.87	-1.46	-0.93	-0.48	-0.01	-0.05	0.01	-0.01

The table includes: the sample name; the soil horizon; the number of analyses (n); mean Hg isotopic signatures of soil and rock samples; and (at the bottom) standard reference materials.



**Extended Data Table 4 | Hg stable isotope compositions of soil samples along a transect to the Arctic Ocean along the Dalton Highway**

name	horizon	Lat (°N)	Lon (°E)	AO (km)	n	$\delta^{204}\text{Hg}$ (‰)	$\delta^{202}\text{Hg}$ (‰)	$\delta^{201}\text{Hg}$ (‰)	$\delta^{200}\text{Hg}$ (‰)	$\delta^{199}\text{Hg}$ (‰)	$\Delta^{204}\text{Hg}$ (‰)	$\Delta^{201}\text{Hg}$ (‰)	$\Delta^{200}\text{Hg}$ (‰)	$\Delta^{199}\text{Hg}$ (‰)
DHWT_S3_Oe	O	69.074	-148.759	137	1	-1.86	-1.33	-1.20	-0.71	-0.52	0.12	-0.20	-0.04	-0.19
DHWT_S3_Oa	O	69.074	-148.759	137	2	-1.54	-1.11	-1.11	-0.56	-0.61	0.11	-0.28	-0.01	-0.33
DHWT_S3_B	A	69.074	-148.759	137	3	-1.50	-1.08	-1.00	-0.58	-0.50	0.11	-0.19	-0.04	-0.23
DHWT_S4_Oa	O	69.146	-148.854	130	1	-1.24	-0.89	-0.76	-0.49	-0.38	0.08	-0.10	-0.04	-0.15
DHWT_S4_Bup	B	69.146	-148.854	130	1	-1.90	-1.26	-1.00	-0.68	-0.41	-0.01	-0.05	-0.04	-0.09
DHWT_S4_Bmid	B	69.146	-148.854	130	1	-1.33	-0.77	-0.67	-0.39	-0.23	-0.19	-0.09	-0.01	-0.04
DHWT_S7_Oe	A	69.991	-148.692	36	2	-1.50	-1.05	-0.80	-0.56	-0.20	0.07	-0.01	-0.04	0.06
DHWT_S7_A_upper	A	69.991	-148.692	36	1	-1.67	-1.16	-0.87	-0.58	-0.29	0.06	0.00	0.00	0.00
DHWT_S_A_lower	A	69.991	-148.692	36	1	-1.64	-1.05	-0.81	-0.56	-0.27	-0.07	-0.02	-0.03	-0.01

The table shows: the sample name; the soil horizon; the latitude and longitude of the sample; the distance to the Arctic Ocean (AO); the number of analyses (*n*); and the mean Hg isotopic signatures of the samples.

Extended Data Table 5 | Stable isotope ratios of precipitation (snow) samples

name	date	amount (ng)	concn (ng L <sup>-1</sup> )	Lat (°N)	Lon (°E)	AO (km)	yield (%)	n	$\delta^{204}\text{Hg}$ (‰)	$\delta^{202}\text{Hg}$ (‰)	$\delta^{201}\text{Hg}$ (‰)	$\delta^{200}\text{Hg}$ (‰)	$\delta^{199}\text{Hg}$ (‰)	$\Delta^{204}\text{Hg}$ (‰)	$\Delta^{201}\text{Hg}$ (‰)	$\Delta^{200}\text{Hg}$ (‰)	$\Delta^{199}\text{Hg}$ (‰)
<b>Samples Toolik Field station</b>																	
TLK_snow_1	29.01.16	9.8	0.5					1	-0.10	-0.11	0.15	0.00	0.13	0.07	0.23	0.05	0.16
TLK_snow_2	29.01.16	7.8	0.4					1	-0.13	-0.27	-0.05	-0.12	0.04	0.27	0.15	0.02	0.10
TLK_snow_3	24.03.16	249.3	12.5					3	-0.40	-0.33	-0.37	-0.12	-0.19	0.09	-0.12	0.05	-0.10
TLK_snow_4	24.03.16	47.6	2.4					2	-0.05	0.01	-0.22	0.01	-0.21	-0.05	-0.22	0.01	-0.21
TLK_snow_5	25.03.16	13.3	0.7					1	0.99	0.74	0.71	0.35	0.38	-0.11	0.16	-0.02	0.20
TLK_snow_15	30.03.16	41.5	2.1					2	-0.39	-0.26	-1.52	-0.11	-1.43	0.00	-1.32	0.02	-1.37
TLK_snow_16	02.04.16	47.2	2.6					2	0.60	0.39	-0.51	0.16	-0.79	0.02	-0.80	-0.03	-0.88
<b>Samples Dalton Highway transect</b>																	
DHWT_snow_7	27.03.16	17.99	0.90	-148.866	68.761	173		2	0.52	0.31	-0.25	0.07	-0.43	0.05	-0.49	-0.09	-0.51
DHWT_snow_8	27.03.16	20.38	1.02	-148.826	69.034	142		2	0.18	0.08	-0.43	0.01	-0.53	0.06	-0.49	-0.03	-0.55
DHWT_snow_9	27.03.16	7.51	0.38	-148.669	69.421	99		1	0.92	0.56	0.03	0.26	-0.32	0.09	-0.39	-0.02	-0.46
DHWT_snow_10	27.03.16	15.25	0.87	-148.605	69.569	82		1	0.17	0.12	-0.27	0.12	-0.34	-0.02	-0.36	0.05	-0.38
DHWT_snow_11	28.03.16	8.07	0.40	-148.613	69.674	70		3	0.83	0.60	-0.05	0.28	-0.47	-0.07	-0.51	-0.02	-0.62
DHWT_snow_13	28.03.16	20.68	1.18	-148.680	70.003	35		2	1.06	0.68	-1.98	0.25	-2.57	0.05	-2.49	-0.09	-2.74
DHWT_snow_14	28.03.16	18.90	1.02	-148.490	70.132	20		3	0.61	0.35	-1.31	0.10	-1.65	0.09	-1.57	-0.08	-1.74
DHWT_snow_17	28.03.16	31.22	3.12	-148.490	70.132	20		2	0.01	0.02	-1.46	-0.05	-1.57	-0.01	-1.47	-0.06	-1.57
<b>Standards</b>																	
processblank_1	05.04.16	2.5	0.12														
processblank_2	24.05.16	0.7	0.07														
processblank_3	24.05.16	1.1	0.08														
NIST-3133_1	25.05.16	17.6	1.76				118	1	0.54	0.22	0.20	0.16	0.04	0.22	0.04	0.05	-0.02
NIST-3133_2	25.05.16	22.6	1.26				113	2	0.00	-0.01	0.03	-0.02	0.01	0.02	0.04	-0.01	0.01

The table includes: the sample name; the date of collection; the amount of Hg in the sample; the Hg concentration (calculated from the recovered Hg mass); the number of analyses (*n*); and the mean Hg isotopic signatures. Samples affected by, and collected during, active AMDEs are marked in grey. Sample 5 consisted of old snow at the bottom of the snow profile, collected during the period when AMDEs occurred. The Hg concentration of process blanks and procedural standards (using bracketing standard NIST-3133) are shown with sample yield and measured Hg isotopic composition.